

# Qualitative analysis of scanning gate microscopy on epitaxial graphene

**Mackenzie, David; Panchal, Vishal; Corte-Leon, Hector; Petersen, Dirch Hjorth; Kazakova, Olga**

*Published in:*
2D materials

*Link to article, DOI:*
10.1088/2053-1583/ab0572

*Publication date:*
2019

*Document Version*
Publisher's PDF, also known as Version of record

**PAPER** • **OPEN ACCESS**

# Qualitative analysis of scanning gate microscopy on epitaxial graphene

To cite this article: David M A Mackenzie *et al* 2019 *2D Mater.* **6** 025023



2D Materials

OPEN ACCESS

RECEIVED
25 October 2018

REVISED
25 January 2019

ACCEPTED FOR PUBLICATION
8 February 2019

PUBLISHED
28 February 2019



PAPER

# Qualitative analysis of scanning gate microscopy on epitaxial graphene

David M A Mackenzie[1,2,5], Vishal Panchal[3,5], Héctor Corte-León[3], Dirch H Petersen[1,4] and Olga Kazakova[3]

[1] Center for Nanostructured Graphene, Technical University of Denmark, Lyngby 2800 Kgs, Denmark
[2] Department of Electronics and Nanoengineering, Aalto University, PO Box 13500, FI-00076 Aalto, Finland
[3] National Physical Laboratory, Teddington, TW11 0LW, United Kingdom
[4] Department of Physics, Technical University of Denmark, Lyngby, Denmark
[5] These authors have contributed equally to the work.

**E-mail:** david.mackenzie@aalto.fi **and** olga.kazakova@npl.co.uk

**Keywords:** scanning gate microscopy, epitaxial graphene, finite element simulations, KPFM, electric field effect, electrical sensitivity

Supplementary material for this article is available online

## Abstract

We present scanning gate microscopy (SGM) studies of graphene Hall-cross devices where bi-layer graphene (2LG) regions show unexpected signal inversion relative to single-layer graphene (1LG), an observation reproduced via finite element modelling of the current densities. This is attributed to gate-induced charge carrier redistribution between the two layers in 2LG. Hall cross devices were fabricated from epitaxial graphene 6H–SiC(0 0 0 1) and were covered by 1LG/2LG with the area ratio of 85:15%, respectively. Local electric-field sensitivity maps of the devices were obtained in two different measurement geometries using electrical SGM with a conductive tip, where it was observed that the voltage of 2LG islands was inverted relative to anticipated reference maps. Finite element modelling of the current densities and voltage response showed good qualitative agreement with the SGM maps when the effect of the gate was reversed for 2LG. The behaviour is attributed to gate-induced charge carrier redistribution between the two layers in 2LG. The model can be used generally as a tool to predict mixed 1LG/2LG response to electric field. Moreover, regions near the corners of the device show the highest sensitivity when the local electric field was applied to the scanning probe microscopy tip. These regions are capable of detecting highly local electric fields down to 110 kV cm$^{-1}$.

## 1. Introduction

Over a decade on, graphene remains a hot topic amongst other 2D-materials, with significant amount of research devoted towards bandgap engineering. Whilst obtaining a large enough bandgap for digital electronics has so far proven to be difficult [1–5], the unique properties of graphene have shown great promise for ultra-high frequency analogue electronics [6], resistance metrology [7], gas sensors [8–10], magnetic field calibration [11], and other applications that do not require a bandgap (e.g. physical barriers) [12]. Applications that require a large number of devices to behave precisely can benefit greatly from large-scale uniformity of number of the graphene layers. However, the fact remains that single crystal and uniform single-layer graphene (1LG) over millimetre scale has yet to be achieved. For example, epitaxial graphene on SiC(0 0 0 1) contains either islands of bi-layer graphene (2LG) on terraces or long thin strips of 2LG running along the terrace edges [13, 14]. Inevitably, fabrication of nanoscale structures on such samples will lead to devices formed from either 1LG or 2LG, or a mixture of 1LG and 2LG [15]. Due to the additional interlayer interactions and electric field screening in 2LG [15, 16], their exact shape, size and location have been shown to greatly alter the performance of devices in applications such as resistance metrology [17–19] and environmental sensors [20–23].

In general, the effects from these types of localised features are difficult to study with standard transport measurements alone as the extracted electrical parameters are averaged over the entire device area. However, there are several techniques which allow spatial mapping of the transport parameters of graphene. These include scanning tunnelling microscopy (STM), microwave microscopy (MM), terahertz time-domain

spectroscopy (THz-TDS) and scanning gate microscopy (SGM).

STM uses a high-aspect ratio metallic cantilever/tip positioned very close to a target substrate so that tunnelling can occur [24], with measurements of graphene directly on SiC demonstrated [25]. Using this technique both local topography and density of states can be mapped. STM can provide atomic resolution of graphene [26], including the transport properties [27], with the density of states/carrier density as a map, as well as extraction of Landau level spectra [28]. Although STM provides the most spatially precise transport measurements available, ideal conditions require ultra-high vacuum as well as special sample preparation to remove all surface contaminates. As a consequence, the properties of graphene devices in ambient are not assessable. In addition, the method is problematic for biased devices, and the scanning area and measurement speed impose a limit to the area probed to a few square microns.

MM uses near-field microwave radiation to extract the conductivity of thin films [29], with conductivity measurements of graphene on polymer [30] and graphene on SiC demonstrated [31]. The measurements can be performed in ambient conditions at a high speed, and over large areas. However, the measurement uncertainty is largely dependent on the graphene coverage percentage [31], and requires a well-calibrated substrate [32]. Other properties of graphene can also be determined using MM such as relative permittivity [33].

THz-TDS is a non-contact method which determines transport properties via the interpretation of how graphene absorbs terahertz radiation [30], with full-wafer maps of graphene on SiC demonstrated [34]. Traditional transmission-mode requires a substrate with high resistivity [35], excluding highly doped Si. However, reflection-mode THz-TDS has shown to provide transport properties equivalent to transmission-mode [36], and graphene-on-polymer mapping removes the wafer requirement altogether [37]. However, as the THz beam spot-size is relatively large, this limits the spatial resolution of THz-TDS to a few hundred microns. In addition, the large number of carriers in metal saturates the signal from graphene, so THz-TDS measurements cannot be performed in the vicinity of metallic electrodes i.e. within approximately 1.2 mm (in the 0.25–1.2 THz range), see [38], which excludes THz-TDS from measuring small-scale devices with metal contacts.

A preferred solution is SGM, a technique that applies a voltage to a conductive atomic force microscopy (AFM) tip and uses it as a localised electrical top gate, thus offering a map of the transport properties with nanometre scale spatial resolution [39–42]. The method has a larger scanning speed and scanning area in comparison to as STM, with scan dimensions of 100 s of microns. Due to tip degradation at high voltages and surface modification issues [43], the gate bias range is limited, however the close proximity of the tip to the surface provides very high electric fields. SGM also has the advantage of being able to be performed in the vicinity of metal contacts, as well as in ambient conditions, with no ultra-clean pre-treatments required. In the graphene community, SGM has been used, e.g. to study charge inhomogeneity caused by the underlying $Si/SiO_2$ substrate [41, 44, 45]. In our previous work, we used SGM to investigate the effectiveness of a top gate on the resistance of 1–2LG devices and reported a significant amount of electric field screening by the 2LG islands present on the current carrying channel of a device [15].

In this work, we use SGM to study the local electrical effects that *AB*-stacked 2LG islands generate in epitaxial 1LG Hall cross devices. We also develop an analytical framework for detailed interpretation of SGM measurements. We map the sensitivity to a local electric field by measuring the voltage response of the Hall cross in transverse (Hall) and longitudinal (bend resistance) geometry [46, 47], and we compare these to the sensitivity obtained from equivalent finite element simulations of the spatial current density. We observe an abrupt change in voltage response when locally gating on 2LG islands compared to 1LG. We demonstrate that the physical location, shape and size of the 2LG islands on a graphene device can significantly alter the electrical response of the device. This manifests from interactions with the electric field of 1LG and 2LG, and the ability of the SGM tip bias to manipulate the carrier density (screening effect and lower carrier mobility of 2LG). The most sensitive parts of the Hall cross are able to detect local electric fields down to 110 kV $cm^{-1}$ in our experimental setup.

## 2. Methods

### 2.1. Sample preparation

The epitaxial graphene was synthesized on semi-insulating 6H–SiC(0 0 0 1) via sublimation of Si from the substrate. Prior to the epitaxial growth, damage from polishing was removed by annealing the substrate at 1580 °C under $H_2$ at 100 mbar. The $H_2$ was then substituted with Ar, while maintaining 100 mbar and 1580 °C [48]. The synthesis was completed within 25 min, after which the sample was cooled to 800 °C while maintaining the Ar atmosphere. This specific route of synthesis produced nominally 1LG with micron scale patches of *AB*-stacked 2LG [16].

The 5 $\mu$m-wide Hall bar devices were fabricated using a three-step process. First step involved electron beam lithography (EBL) with PMMA and ZEP520 resists, reactive ion etching (RIE) with oxygen and electron beam physical vapour deposition (EBPVD) of Cr/Au (5/100 nm) to define contact pads that are well-adhered to the substrate. Second step involved EBL and EBPVD of Cr/Au to define the electrical leads. Third step involved EBL and RIE to define the Hall bar devices.

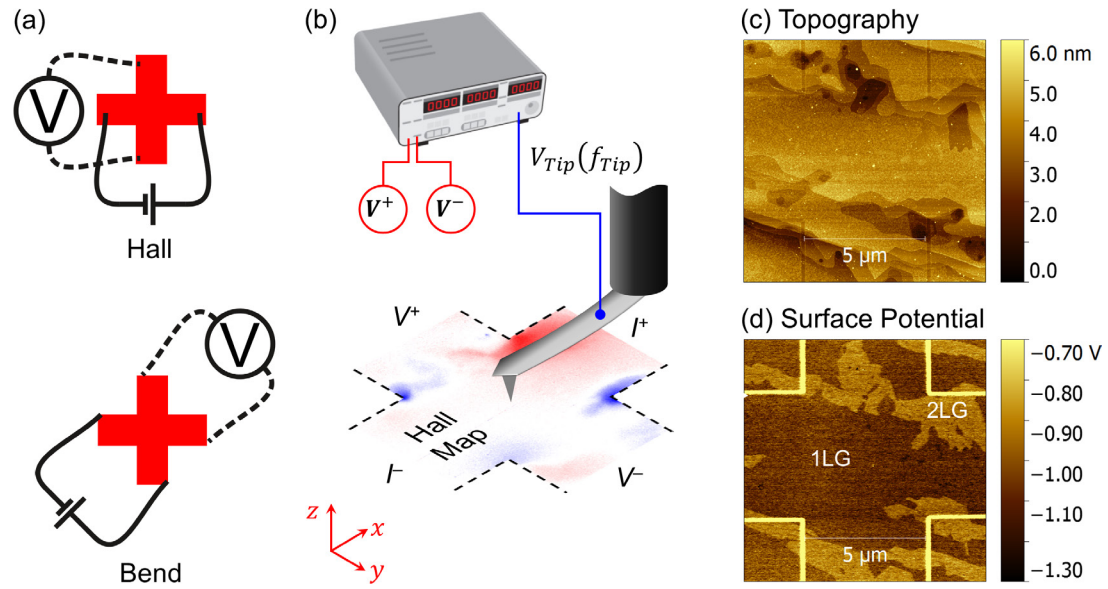


**Figure 1.** (a) Hall and bend resistance measurement geometries. (b) Schematic of scanning gate microscopy measurement setup. The colour map shows SGM image in the Hall geometry. (c) Topography and (d) surface potential maps showing the single-layer (1LG) and bi-layer graphene (2LG) distribution across the 5 $\mu$m-wide Hall bar device.

### 2.2. Electrical scanning gate microscopy

The electrical SGM was carried out using the NT-MDT NTEGRA Aura scanning probe microscope (SPM) in ambient air at standard temperature and pressure. Doped Si tips with nominal resonant frequency of $f_0 = 300$ kHz, apex radius of 10 nm and spring constant, $k = 0.8$ N m$^{-1}$ (PFQNE-AL by Bruker) were used. The SGM measurements were performed at the same time as AFM. During the standard non-contact mode AFM, where the topography of the sample is tracked by oscillating the tip at $f_0$ and maintaining root mean square (RMS) tip-sample distance of 6 nm, a low frequency ($f_{Tip} = 97$ Hz) AC voltage ($V_{Tip}$) was applied to the tip using the sine wave output of an external lock-in amplifier (LIA, Stanford Research Systems SR830). $V_{Tip}$ was kept to a maximum of 5 V in order to avoid local oxidation of graphene due to interaction with the tip and surface water [43] and degradation of the probe apex. By applying an additional DC bias current across the device ($I_{Bias}$), the AC electric field emanating from the tip apex induced an AC voltage response in the Hall ($V_{XY}$) and bend ($V_{XX}$) geometry (figure 1(a)). The response of the device was measured simultaneously with the LIA referenced to $f_{Tip}$ and recorded by the SPM to build a voltage map in Hall and bend geometry (figure 1(b)).

The response of the device was characterised by performing spectroscopy at specific locations of the device. This consisted of using the AFM feedback to maintain the tip-sample distance and hold the tip stationary in $x$-$y$ plane, during which time the $V_{Tip}$ was either swept (from 0–5 V) or applied in a step-wise manner (10–25 mV increments), while measuring $V_{XY}$ and $V_{XX}$.

### 2.3. Simulations

We can qualitatively evaluate the SGM measurements by use of a sensitivity analysis similar to studies of the general interpretation of four-terminal measurements [49, 50]. The change in measured voltage $\Delta V_m$ can be derived [51] by considering a small perturbation of local sheet carrier density $N_S$ induced by the gate bias on the AFM tip and the corresponding sensitivity to this perturbation governed by the equation:

$$\Delta V_m = -\frac{Z}{\mu N_S^2}\frac{C_{Tip}V_{Tip}}{e^2 I}\mathbf{J}_s \cdot \widetilde{\mathbf{J}}_s. \qquad (1)$$

Here, $Z$ is the local carrier type (1 or $-1$ for holes and electrons respectively), $\mu$ is the local carrier mobility, $C_{Tip}$ is the tip-sample capacitance, $e$ is the electronic charge, $I$ is the current applied to the device, $\mathbf{J}_s$ is the sheet current density in the device and $\widetilde{\mathbf{J}}_s$ the current density in the reciprocal configuration (i.e. where current and voltage electrodes are interchanged).

In reality, the sheet carrier density is modulated in the entire device as the electric field between tip and sample is not limited to the vicinity of the AFM tip. Thus, the absolute value of $C_{Tip}$ is ill defined, but serves well for a *qualitative* assessment. For the full quantitative analysis, the electric field normal to the sample surface must be evaluated for each location of the AFM tip as well as the cantilever. This three-dimensional analysis is beyond the scope of this study.

Finite-element simulations (FES) were performed with COMSOL Multiphysics 5.3 using a 2D model with the physics package *Electric Currents* in the stationary regime. Device geometry was defined by importing the 1LG and 2LG regions from the topography and surface potential maps shown in figures 1(c) and (d). 1LG and

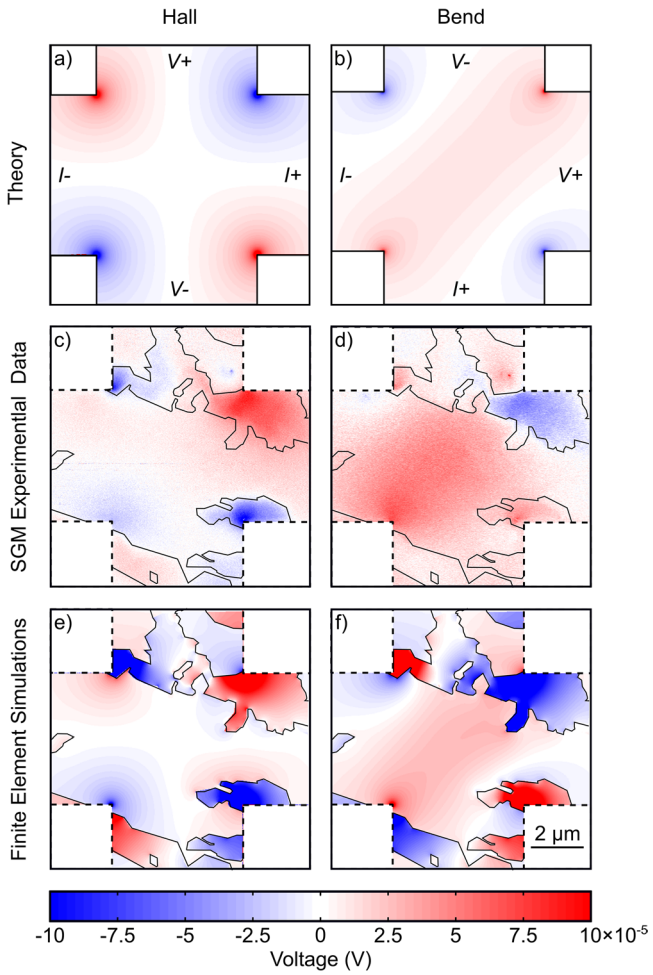


**Figure 2.** Theoretical reference maps for electrical SGM on a 5 $\mu$m-wide homogeneous 1LG (no 2LG islands) Hall bar device in (a) Hall and (b) bend geometry with current and voltage pins marked. Experimental electrical SGM images in (c) Hall and (d) bend geometry for the 5 $\mu$m-wide epitaxial graphene Hall bar device shown in figure 1. The maps are 10 × 10 $\mu$m$^2$ and were obtained with $V_{Tip} = 5$ V ($E \approx 28$ MV cm$^{-1}$), $f_{Tip} = 97$ Hz and $I_{Bias} = 75$ $\mu$A. (e) Hall and (f) bend geometry voltage maps ($\Delta V_m$) simulated using FES for the same device as in (c) and (d).

2LG were designated as distinct materials with different sheet conductance. The simulations were performed for the Hall and bend geometries, as shown in figure 1(a), as well as their reciprocal geometries. The $x$ and $y$ components of current density ($J_x$, $J_y$) for both geometries were exported to MATLAB, and voltage maps were calculated in accordance with equation (1).

For the FES, the only variable was the ratio between the conductance of the 1LG and 2LG, and for calculations of $\Delta V_m$ values, $\mu$, $N_S$, $C_{Tip}$, $I$ and $V_{Tip}$ are selected to correspond to experimentally determined values, and the corresponding conductance ratio used in the FES.

## 3. Results and discussion

### 3.1. Device topography and transport properties

The 5 $\mu$m-wide Hall cross was first imaged with AFM and frequency modulated Kelvin probe force microscopy (FM-KPFM) to determine the topography and graphene layer thickness (figures 1(c) and (d), respectively) [52]. From these SPM images, confocal optical intensity [53] and Raman mapping (supplementary figure S1 (stacks.iop.org/TDM/6/025023/mmedia)), and our previous work on epitaxial grapheme [15, 21], we identified the Hall cross to consist of 85% 1LG and 15% 2LG (darker and brighter regions, respectively, in figure 1(d)). The transport properties of the Hall cross were characterised in ambient environment with the Hall effect and 4-point resistance measurements described in [15]. Using these techniques, the average electron carrier density and mobility, and sheet resistance were determined as $n_e = 8.3 \times 10^{11}$ cm$^{-2}$, $\mu_e = 1500$ cm$^2$ V$^{-1}$ s$^{-1}$, and $R_s = 5014\,\Omega$, respectively.

### 3.2. SGM response to 1LG and 2LG

During SGM, the local carrier density is perturbed by the local electric field emanating from the tip. In the Hall geometry, the simulated reference map (figure 2(a)) shows that inherently a uniform 1LG device has zero response to the local electric field [54] when the tip is at the horizontal and vertical symmetry axis of the cross and positive/negative response at corners of the cross with a two-fold symmetry along the diagonal axis of the cross. The positive/negative voltage response is the result of the locally perturbed sheet conductance. For the bend geometry, the simulated reference map

(figure 2(b)) for a uniform 1LG device also shows a two-fold symmetry along the diagonal axis of the cross; with the additional positive band that spans from bottom left to top right corner. Both geometries are consistent with previous results on semiconductor devices [55, 56].

Figures 2(c) and (d) show the experimental voltage map in Hall and bend geometry, respectively, in response to the local electric field generated by applying $V_{Tip} = 5$ V RMS to the tip. During the scans, the device was current biased at $I_{Bias} = 75\ \mu$A and the tip-sample distance was $r = 6$ nm, producing maximum electric field strength of $E = \frac{2aV_{Tip}}{r^2} \sim 28$ MV cm$^{-1}$, where $a$ is tip radius. The tip capacitance was estimated as $\approx$1.6 aF, following the formalism developed in [57] and shown in detail in Supplementary Information.

On the 1LG parts of the device, both experimental maps are consistent with the simulated reference maps (figures 2(a) and (b)). For example, in the Hall (bend) geometry, the bottom left corner of the device shows negative (positive) signal and the centre of the device shows zero (positive) signal. However, when the tip is gating in the region of 2LG islands, the measured signal shows a clear sign-change relative to the simulated reference maps. Moreover, the magnitude of the signal is generally larger for 2LG located in the active part of the Hall cross and especially when gating near edges or constrictions due to geometry related electric field enhancements. All the above features observed in Hall and bend geometry maps are also subject to 180° rotational symmetry when current and voltage lead configurations are rotated by 180° (supplementary figure S2), consistent with the reciprocity theorem. Additional SGM measurements performed on a different non-uniform 5 $\mu$m-wide epitaxial graphene device under identical experimental conditions (supplementary figure S3), show similar features in Hall and bend geometry to those in figures 2(a) and (b), respectively, including the inversion of signal for 2LG regions.

To understand the inversion in the signal by 2LG islands, we use the simulation method described in section 2.3. Due the predominance of 1LG in the device, the simulated 1LG was set to match the experimentally observed transport parameters of $n = 8.3 \times 10^{11}$ cm$^{-2}$, $\mu = 1500$ cm$^2$ V$^{-1}$ s$^{-1}$, and with a number of carriers ratio $n_{2LG}/n_{1LG}$ of 4 based on previous experimental work [15]. For the calculation of the current densities, only the resistance ratio between the layers was varied. The other experimental parameters ($I$, $V_{Tip}$) were subsequently used with a $C_{Tip}$ of 1.6 aF (as estimated in supplementary information) to create a spatial map of $\Delta V_m$ using equation (1). A least squared fit was then used to determine the optimum resistance ratio, found to be $\sigma_{1LG}/\sigma_{2LG} = 2$. Because $n_{2LG}/n_{1LG}$ and $\mu_{1LG}$ are defined, this pegs the value of $\mu_{2LG}$ to $\mu_{1LG}/2$.

A good qualitative agreement between the experimental data (figures 2(c) and (d)) and FES results (figures 2(e) and (f)) was found only in assumption that $Z$ was negative for 2LG and positive for 1LG. We observe that $\Delta V_m$ for experiment and simulation are similar both spatially and in magnitude. We note that the one area where the simulations and experimental data diverge is the bottom left hand corner of figure 2(f). For 2LG in this region the experimental data is slightly positive while the simulation data is negative. The explanation is that the cantilever adds an overall positive global effect to the measured signal for the bend configuration. In the bend configuration, the overall expected signal is positive (figure 2(a)). As the device is predominantly 1LG, so when the tip is locally probing the 2LG area in the bottom left corner, the tip will contribute with a negative component to the measured signal, and because the global effect from the cantilever is primarily gating 1LG, it will contribute a positive signal. The two effects almost cancel each other out, resulting that the 2LG area in the lower left corner of figure 2(f) is slightly positive. Because our simulations are only capable of modelling the tip, this overall offset is not observed in figure 2(f). In addition, the 1LG areas of figure 2(d) show an overall positive offset with respect to the reference map, which is attributed to this cantilever effect. We also observe that the tip-cantilever effect is dependent on the size of 2LG islands. In an area with larger coverage of 2LG (e.g. upper right corner of figure 2(d)), we observe a smaller opposite-sign contribution from surrounding 1LG areas, and corresponding better agreement with the simulations compared to the smaller 2LG islands in the left/lower left hand corner.

Alternatively, the Hall configuration was not affected by this offset due to the symmetry of the sensitivity reference map, which leads to a more accurate quantitative agreement between the experimental and simulation data.

Figure 3 shows two potential mechanisms explaining opposite response to $V_{Tip}$ for 1LG and 2LG. One interpretation, shown in figures 3(a) and (b), is that charge neutrality points (CNP) of 1LG and 2LG have different values. If each layer has different carriers, (i.e. n-type 1LG and p-type 2LG), then opposite effects will occur under the local gate. This can happen in two ways. Firstly, as shown in figure 3(a), if the tip provides sufficient electric field for the Fermi level to cross the Dirac point, then 2LG becomes p-type under gating conditions. Alternatively, as shown in figure 3(b), if at zero gate bias 1LG is n-type and 2LG is p-type, then the gate would have an opposite effect on each layer for all $V_{Tip}$ values. A second interpretation, shown in figures 3(c)–(f), is that the electric field from the tip causes local surface accumulation of charge in 2LG areas (figure 3(f)).

In order to determine if $V_{Tip}$ leads to switching carriers from n-type to p-type (by crossing the CNP), we measured at points consisting of only 1LG or 2LG and swept the magnitude of $V_{Tip}$ from 0 to 5 V and back. The results are shown in supplementary information figure S4, where we observe a linear increase in signal with tip voltage both for 1LG (figure S4 points A, B)

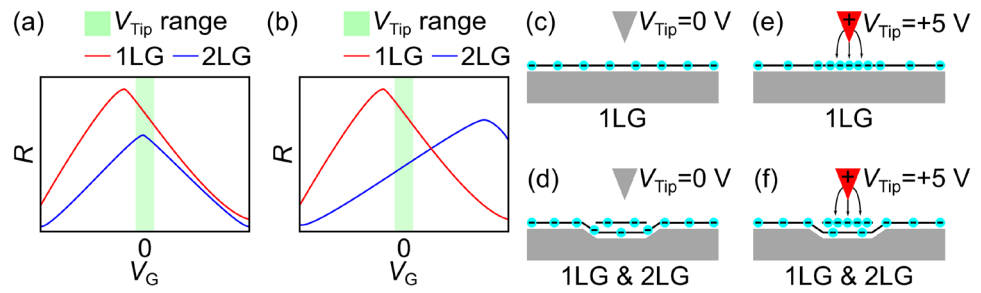


**Figure 3.** Proposed mechanisms for the observed behaviour in 2LG. (a) Schematic of transport properties (lines) and tip gating range (green area) where the tip provides sufficient electric field for the Fermi level to cross the Dirac point such that 2LG is p-type under gating conditions. (b) Schematics of transport properties (lines) and tip gating range (green area), where at zero gate bias 1LG is n-type and 2LG is p-type and the gating range does not pass the Dirac point. (c) and (d) Schematics showing uniform single layer and mixed single/double layer under zero tip bias. Light blue dots represent charge density and triangles represent the SGM tip (e) and (f) Schematic showing uniform single layer and mixed single/double layer under positive tip bias. The electric field from the tip causes surface accumulation of charge.

and 2LG (figure S4 points C, D). This is good evidence that the carrier type is not changed for the tip voltage range 0–5 V that we use for the experiment, as in that case we would expect first to observe an increase in $V_{xx}$ and then a decrease (or vice versa) as the tip voltage passed the CNP.

Based on previous Hall measurements with no tip voltage applied, we also know that both fully 1LG and 2LG covered devices are n-type at $V_G = 0$ [15]. By means of Hall measurements we also observe that the mixed single-double layer devices studied here are of n-type. We therefore conclude that we have n-type carriers in both 1LG and 2LG under non-gating conditions, so we can therefore exclude the mechanism from figures 3(a) and (b).

We now consider the mechanism from figures 3(c)–(f). Figures 3(c) and (d) show 1LG and 2LG for $V_{Tip} = 0$ V, respectively. When the positive gate voltage (+5 V) is applied to the tip (figures 3(e)–(f)), it leads to accumulation of the negative charge. For the case of 2LG, the negative charge accumulates on the top layer. In order for charge accumulation to occur in a system, it assumes that the layers are electrically coupled, and that different carrier concentrations can occur in each layer, known for the case for Bernal-stacked grapheme [58–60]. We can infer that 2LG studied here is Bernal stacked due to the shift in position of the Raman 2D peak for 2LG areas [61], as shown in supplementary information figures S1(b) and (c). Based on this model, due to charge accumulation on the top layer, the area of 2LG under tip will appear as if it is p-type during SGM measurements due to the redistribution of charge within the device, but are in fact always n-type. This matches the experimental data of 2LG switching sign and is consistent with the observations that (i) for zero gating we have n-type for both layers and (ii) no carrier inversion occurs in our gating range.

This mechanism combined with the tip-cantilever analysis above is also consistent with previous measurements of mixed 1LG/2LG Hall bars [15], when evaluated in a different geometry (i.e. measurement of the channel resistance). It was observed that the $V_{xx}$ signal in the centre of a 2LG area was lower in magnitude, however not negative. In the case of 1LG device, gating anywhere along the channel resulted in an increase in the channel resistance due to depletion and redistributions of carriers within the graphene device. For the mixed 1LG/2LG device, gating on the 2LG parts of the channel also resulted in an increase in the channel resistance, however the magnitude was significantly lower than for 1LG part of the device channel. Even for predominantly 2LG devices, the total signal can be small and positive (rather than negative) due to the electric field screening effect of 2LG [14, 15] combined with the more sensitive but small areas of 1LG providing an overall positive signal from the cantilever for all probing locations. This also aides in explaining why the gating effect in 2LG was observed to be 20 times lower than 1LG only in the primarily 2LG device [15]. Each possible mixed-layer device has distinct island size and distribution, which leads to a different combination of the negative (tip/2LG) and positive (cantilever/1LG) components of the overall measured signal. When considering the response of mixed-layer graphene devices to local electric fields in non-symmetrical measurement geometries (such as figure 2(b) and in [15]), it is important to consider the localised gating effect of the tip as well as the topographically-dependent effects of the relative 2LG island size, distribution, and cantilever gating. These effects can be minimised by choosing a symmetrical measurement geometry, and are qualitatively predictable using FES.

### 3.3. Sensitivity to electric fields

The linearity and the detection limit of the device to local electric fields was investigated for Hall and bend geometry by performing spectroscopy at the most sensitive parts of the device on 1LG, i.e. positions 1–3 indicated in figure 4(a). Position 1 is at the centre of the cross and positions 2 and 3 are near top left and top right corners of the cross, respectively. All three chosen locations show good linearity (adjacent $R$-square greater than 99.4% for all the fits) for electric field strengths up to $E \sim 28$ MV cm$^{-1}$ (figure 4(b)). In order to compare these locations with the theoretically most

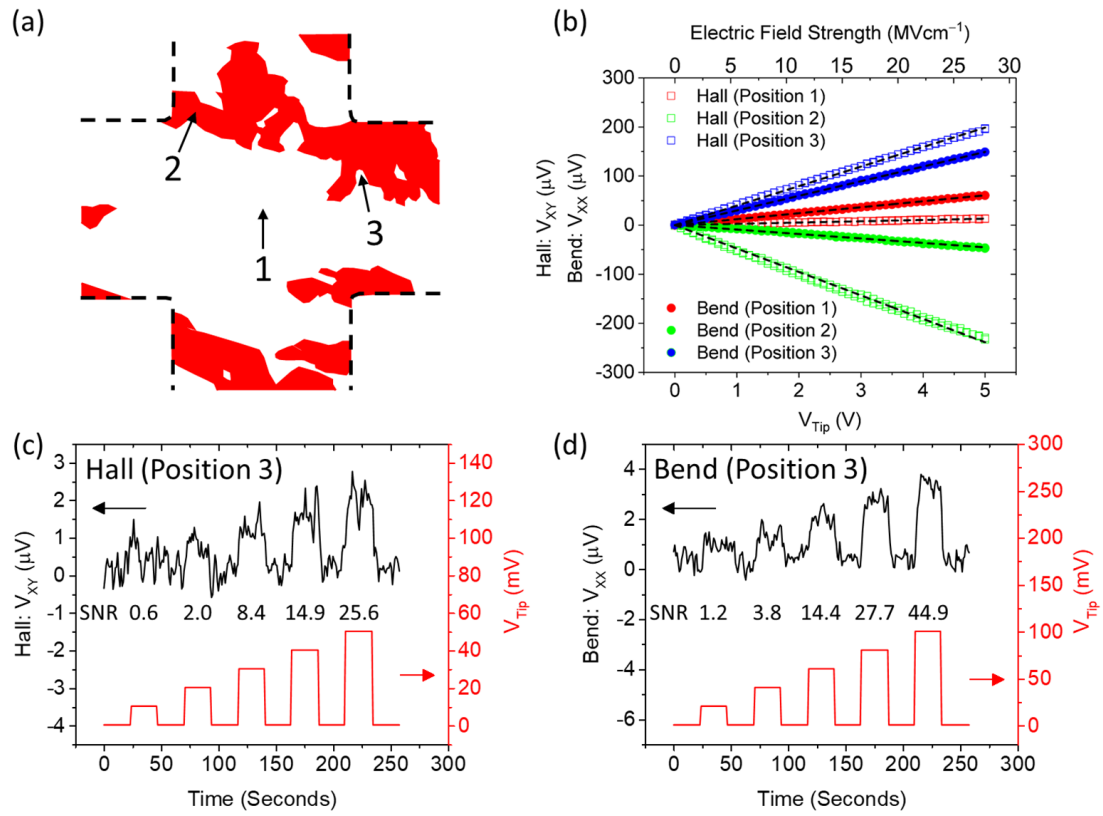


**Figure 4.** (a) Schematic of the device showing spectroscopy locations. (b) The linear dependence of device response in the Hall and bend geometry to a local $V_{Tip}$ ($f_{Tip} = 97$ Hz and $I_{Bias} = 75$ $\mu$A) at positions 1–3 indicated in (a). Dashed black lines are linear fits to the dataset with adjacent $R$-square greater than 99.4% for all the fits. (c) Hall and (d) bend response to a local step-wise change in $V_{Tip}$ ($f_{Tip} = 97$ Hz and $I_{Bias} = 75$ $\mu$A) at position 3 indicated in (a).

sensitive areas of the device, i.e. geometrical corners (figure 2(a)), we show four additional spectroscopy locations, which are located at the corners for the Hall configuration, shown in figure S4(a). We observe approximately 5 times larger signal at the bilayer edges, a maximum $V_{xx}$ signal of |240 $\mu$V| (Position 2 in figure 4(b)), compared to |55 $\mu$V| at the geometrical corners of the device (Position D in figure S4(b)), showing that the sensitivity to electric fields is enhanced at the bilayer edge. Spectroscopy measurements at positions 2 and 3 (figure S4(b)) shows higher signal than the same location in the map in figure 2(d) due to the lower spatial resolution of the map. Spectroscopy at position 3 (figure 4(b)) was also carried out at $I_{Bias} = 0$, 25, 50 and 75 $\mu$A for Hall and bend geometries showing good linearity with increasing bias current (supplementary figure S5). Next, the response of the local area was determined by applying $V_{Tip}$ in a step-wise and incremental manner for the Hall and bend geometry. At the centre of the cross, i.e. position 1 (supplementary figure S6(a)), the Hall geometry is only sensitive to fields greater than $E \sim 1.1$ MV cm$^{-1}$ ($V_{Tip} = 200$ mV), but sensitivity in bend geometry improves by factor of four to $E \sim 280$ kV cm$^{-1}$ ($V_{Tip} = 50$ mV). At position 2, the minimal changes in $V_{XY}$ and $V_{XX}$ were identifiable for fields larger than $E \sim 110$ kV cm$^{-1}$ ($V_{Tip} = 20$ mV) and $E \sim 550$ kV cm$^{-1}$ ($V_{Tip} = 100$ mV), for Hall and bend geometries, respectively (supplementary figure S6(b)). At position 3, the highest value of sensitivity is achieved at $E \sim 110$ kV cm$^{-1}$ ($V_{Tip} = 20$ mV) in both Hall and bend geometries (figures 4(c) and (d), respectively). The sensitivity of these devices to external out-of-plane electric fields demonstrated here are comparable to those achieved in traditional parallel plate back- or top-gated systems [2], however in the present case, the sensitivity arises from a highly local electric field.

Using the step-wise change in $V_{XY}$ and $V_{XX}$, the signal-to-noise (SNR) ratio was estimated with $\mathrm{SNR} = \left[\frac{\bar{V}(V_{Tip}) - \bar{V}(V_{Tip}=0)}{\sigma(V_{Tip}=0)}\right]^2$, where $\bar{V}$ is $V_{XY}$ and $V_{XX}$ for Hall and bend geometry, respectively, and $\sigma$ is the standard deviation of $V_{XY}$ and $V_{XX}$ at $V_{Tip} = 0$. Figure 5 shows the relation of SNR with $V_{Tip}$ for all three positions indicated in figure 4(a). The steepness of the gradient gives a clear indication of the most active parts of the device. For example, in the Hall geometry, positions 2 and 3 (which are near the corners of the device, surrounded by 2LG) exhibit the highest SNR, whereas position 1 (centre of the cross) is the least sensitive part (~30 times less sensitive than the corners). For the bend geometry, position 3 offers the best sensitivity. Although we demonstrate screening of external out-of-plane electric fields by 2LG, the spectroscopy measurements also show that current is redirected to the boundary between the 1LG and 2LG, as implied

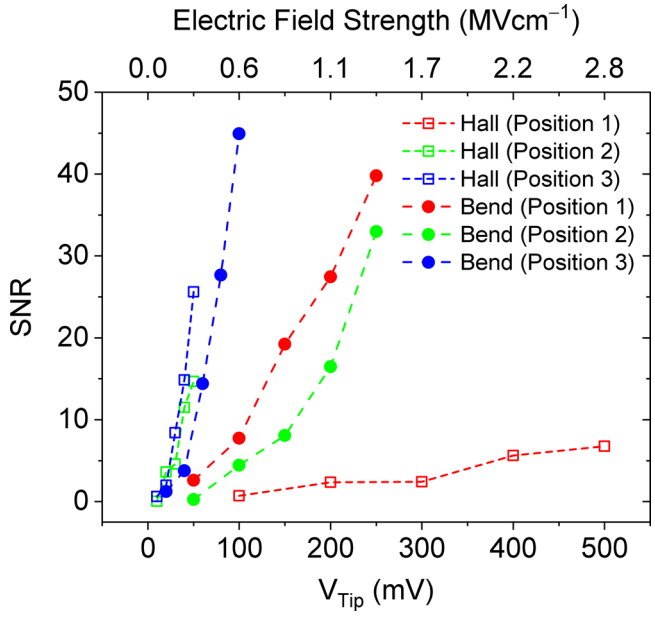


**Figure 5.** The signal-to-noise ratio (SNR) extracted from the step-wise change in $V_{Tip}$ and electric field strength for all three positions in Hall and bend geometry. Lines are the guides for the eye.

by the larger sensitivity in this area. This is due to the lower resistance of the 2LG islands and the associated current crowding based on the island geometry. Therefore, in comparison to an entirely single-layer device the inclusion of 2LG islands helps to redistribute the carriers locally near boundaries, thus giving rise to the higher sensitivity to electric fields for devices with 2LG islands. The sensitivity is further enhanced when the local electrical field from the tip is fully surrounded by edges of 2LG (i.e. positions 2 and 3), which is an analogue to higher sensitivity at the geometrical 90° corners of a cross (i.e. figures 2(a) and (b)).

## 4. Conclusion

In summary, we have investigated local electrical gating effects on 5 $\mu$m-wide Hall cross devices fabricated from non-uniform epitaxial graphene on 6H–SiC(0 0 0 1). Surface potential mapping with FM-KPFM, confocal optical imaging and Raman microscopy revealed the graphene layer structure of the device as 1–2LG. Using electrically conductive tips, SGM was performed in Hall and bend geometries under DC current bias in ambient air. For the Hall geometry, SGM maps reveal strong positive/negative signals at the corners of the cross, with two-fold symmetry and 180° rotational symmetry of the current/voltage measurement leads. In both geometries, locally gating on 2LG islands in the active area of the device inverts the signal. The inversion of the signal on 2LG islands is attributed to charge accumulation on the surface of 2LG, as consistent with the finite element modelling of 1LG and 2LG as distinct materials where $\sigma_{1LG}/\sigma_{2LG} = 2$ and $\mu_{2LG} = \mu_{1LG}/2$. The simulated observed offset voltage qualitatively matches the SGM data as if the material had opposite carrier types although both layers are n-type. For non-symmetrical measurement geometries it is important to consider the interplay of the localised gating effect of the tip as well as the broader effects of the cantilever gating and relative 2LG island size. These effects can be minimised by choosing a symmetrical measurement geometry, and are qualitatively predictable using FES. Additional spectroscopy measurements reveal that most active parts of the graphene device are sensitive to local electric fields down to 110 kV cm$^{-1}$. This was attributed to significant local redistribution of carriers from electric field enhancement by 2LG edges. Thus, we show that SGM is an effective tool for studying electrical gating effects in devices with tens-of-nanometre scale spatial resolution. Strategic device design with specific 2LG structures can be used to enhance sensitivity of devices to electric fields. Moreover, using a sensitivity analysis allows for qualitative assessment of transport properties.

## Acknowledgments

The work has received funding from the European Union's Horizon 2020 research and innovation programme under grant agreement GrapheneCore2 785219 number. Additionally, the experimental work at the National Physical Laboratory was supported by the UK government's Department for Business, Energy and Industrial Strategy and the Joint Research Project 16NRM01 GRACE: Developing electrical characterisation methods for future graphene electronics. The theoretical modelling at Centre for Nanostructured Graphene was supported by Danish National Research Foundation (project DNRF103 CNG) as well as H2020 European Project No. 692527. Authors would like to thank R L Myers-Ward and D K Gaskill for growth of epitaxial graphene and A Lartsev

for fabrication of devices, as well as A Tzalenchuk and N Huang for useful discussions.

## ORCID iDs

David M A Mackenzie https://orcid.org/0000-0003-1114-2955
Vishal Panchal https://orcid.org/0000-0003-3954-8535
Héctor Corte-León https://orcid.org/0000-0002-2037-8292
Olga Kazakova https://orcid.org/0000-0002-8473-2414

## References

[1] Zhou S Y, Gweon G-H, Fedorov A V, First P N, de Heer W A, Lee D-H, Guinea F, Castro Neto A H and Lanzara A 2007 Substrate-induced bandgap opening in epitaxial graphene *Nat. Mater.* **6** 770–5
[2] Zhang Y, Tang T-T, Girit C, Hao Z, Martin M C, Zettl A, Crommie M F, Shen Y R and Wang F 2009 Direct observation of a widely tunable bandgap in bilayer graphene *Nature* **459** 820–3
[3] Schwierz F 2010 Graphene transistors *Nat. Nanotechnol.* **5** 487–96
[4] Mackenzie D M A, Cagliani A, Gammelgaard L, Jessen B S, Petersen D H and Bøggild P 2017 Graphene antidot lattice transport measurements *Int. J. Nanotechnol.* **14** 226
[5] Jessen B S *et al* 2019 Lithographic band structure engineering of graphene *Nat. Nanotechnol.* (https://doi.org/10.1038/s41565-019-0376-3)
[6] Lin Y-M, Dimitrakopoulos C, Jenkins K A, Farmer D B, Chiu H-Y, Grill A and Avouris P 2010 100 GHz transistors from wafer-scale epitaxial graphene *Science* **327** 662
[7] Tzalenchuk A, Lara-Avila S, Kalaboukhov A, Paolillo S, Syväjärvi M, Yakimova R, Kazakova O, Janssen T J B M, Fal'ko V and Kubatkin S 2010 Towards a quantum resistance standard based on epitaxial graphene *Nat. Nanotechnol.* **5** 186–9
[8] Yuan W and Shi G 2013 Graphene-based gas sensors *J. Mater. Chem.* A **1** 10078
[9] Cagliani A, Mackenzie D M A, Tschammer L K, Pizzocchero F, Almdal K and Bøggild P 2014 Large-area nanopatterned graphene for ultrasensitive gas sensing *Nano Res.* **7** 743–54
[10] Mackenzie D M A, Smistrup K, Whelan P R, Luo B, Shivayogimath A, Petersen D H, Messina S A and Bøggild P 2017 Batch fabrication of nanopatterned graphene devices via nanoimprint lithography *Appl. Phys. Lett.* **111** 193103
[11] Panchal V, Corte-león H, Gribkov B, Rodriguez L A, Manzin A, Simonetto E, Vock S, Neu V and Kazakova O 2017 Calibration of multi-layered probes with low/high magnetic moments *Sci. Rep.* **7** 7224
[12] Yu F, Camilli L, Wang T, Mackenzie D M A, Curioni M, Akid R and Bøggild P 2018 Complete long-term corrosion protection with chemical vapor deposited graphene *Carbon* **132** 78–84
[13] Yakimova R, Iakimov T, Yazdi G R, Bouhafs C, Eriksson J, Zakharov A, Boosalis A, Schubert M and Darakchieva V 2014 Morphological and electronic properties of epitaxial graphene on SiC *Physica* B **439** 54–9
[14] Melios C, Panchal V, Giusca C E, Strupinski W, Silva S R P and Kazakova O 2015 Carrier type inversion in quasi-free standing graphene: studies of local electronic and structural properties *Sci. Rep.* **5** 10505
[15] Panchal V, Giusca C E, Lartsev A, Yakimova R and Kazakova O 2014 Local electric field screening in bi-layer graphene devices *Frontiers Phys.* **2** 3
[16] Ohta T, Bostwick A, McChesney J, Seyller T, Horn K and Rotenberg E 2007 Interlayer interaction and electronic screening in multilayer graphene investigated with angle-resolved photoemission spectroscopy *Phys. Rev. Lett.* **98** 16–9
[17] Yager T *et al* 2013 Express optical analysis of epitaxial graphene on SiC: impact of morphology on quantum transport *Nano Lett.* **13** 4217–23
[18] Chua C *et al* 2014 Quantum Hall effect and quantum point contact in bilayer-patched epitaxial graphene *Nano Lett.* **14** 3369–73
[19] Yager T *et al* 2015 Low contact resistance in epitaxial graphene devices for quantum metrology *AIP Adv.* **5** 087134
[20] Giusca C E, Panchal V, Munz M, Wheeler V D, Nyakiti L O, Myers-Ward R L, Gaskill D K and Kazakova O 2015 Water affinity to epitaxial graphene: the impact of layer thickness *Adv. Mater. Interfaces* **5** 1500252
[21] Panchal V, Giusca C E, Lartsev A, Martin N A, Cassidy N, Myers-Ward R L, Gaskill D K and Kazakova O 2016 Atmospheric doping effects in epitaxial graphene: correlation of local and global electrical studies *2D Mater.* **3** 015006
[22] Melios C, Giusca C E, Panchal V and Kazakova O 2018 Water on graphene: review of recent progress *2D Mater.* **5** 022001
[23] Melios C, Panchal V, Edmonds K, Lartsev A, Yakimova R and Kazakova O 2018 Detection of ultralow concentration $NO_2$ in complex environment using epitaxial graphene sensors *ACS Sens.* **3** 1666–74
[24] Andrei E Y, Li G and Du X 2012 Electronic properties of graphene: a perspective from scanning tunneling microscopy and magnetotransport *Rep. Prog. Phys.* **75** 056501
[25] Xu P *et al* 2014 Multilayer graphene, Moire boundaries and defects identified by scanning tunneling microscopy on the *m*-plane, non-polar surface of SiC *Carbon* **80** 75–81
[26] Dimiev A, Kosynkin D V, Sinitskii A, Slesarev A, Sun Z and Tour J M 2011 Layer-by-layer removal of graphene for device patterning *Science* **331** 1168–72
[27] Decker R, Wang Y, Brar V W, Regan W, Tsai H Z, Wu Q, Gannett W, Zettl A and Crommie M F 2011 Local electronic properties of graphene on a BN substrate via scanning tunneling microscopy *Nano Lett.* **11** 2291–5
[28] Li G and Andrei E Y 2007 Observation of Landau levels of Dirac fermions in graphite *Nat. Phys.* **3** 623–7
[29] Imtiaz A, Pollak M, Anlage S M, Barry J D and Melngailis J 2005 Near-field microwave microscopy on nanometer length scales *J. Appl. Phys.* **97** 044302
[30] Bøggild P, Mackenzie D M A, Whelan P R, Petersen D H, Buron J D, Zurutuza A, Gallop J, Hao L and Jepsen P U 2017 Mapping the electrical properties of large-area graphene *2D Mater.* **4** 042003
[31] Hao L, Gallop J, Goniszewski S, Shaforost O, Klein N and Yakimova R 2013 Non-contact method for measurement of the microwave conductivity of graphene *Appl. Phys. Lett.* **103** 10–4
[32] Shaforost O, Wang K, Goniszewski S, Adabi M, Guo Z, Hanham S, Gallop J, Hao L and Klein N 2015 Contact-free sheet resistance determination of large area graphene layers by an open dielectric loaded microwave cavity *J. Appl. Phys.* **117** 024501
[33] Myers J, Mou S, Chen K and Zhuang Y 2017 Scanning microwave microscope imaging of micro-patterned monolayer graphene grown by chemical vapor deposition *Appl. Phys. Lett.* **108** 053101
[34] Whelan P R *et al* 2018 Electrical homogeneity mapping of epitaxial graphene on silicon carbide *ACS Appl. Mater. Interfaces* **10** 31641
[35] Buron J D, Mackenzie D M A, Petersen D H, Pesquera A, Centeno A, Bøggild P, Zurutuza A and Jepsen P U 2015 Terahertz wafer-scale mobility mapping of graphene on insulating substrates without a gate *Opt. Express* **23** 30721
[36] Mackenzie D M A, Whelan P R, Bøggild P, Jepsen P U, Redo-Sanchez A, Etayo D, Fabricius N and Petersen D H 2018 Quality assessment of terahertz time-domain spectroscopy transmission and reflection modes for graphene conductivity mapping *Opt. Express* **26** 9220

[37] Whelan P R, Huang D H, Mackenzie D M, Messina S, Chancheng Z L, Lunqing Y L, Booth T J, Jepsen P U and Boggild P 2018 Conductivity mapping of graphene on polymeric films by terahertz time-domain spectroscopy *Opt. Express* **26** 17748–54
[38] Mackenzie D M A, Buron J D, Boaggild P, Jepsen P U and Petersen D H 2016 Contactless graphene conductance measurements: the effect of device fabrication on terahertz time-domain spectroscopy *Int. J. Nanotechnol.* **13** 591
[39] Soudi A, Aivazian G, Shi S-F, Xu X D and Gu Y 2012 Probing transconductance spatial variations in graphene nanoribbon field-effect transistors using scanning gate microscopy *Appl. Phys. Lett.* **100** 033115
[40] Garcia A G F, König M, Goldhaber-Gordon D and Todd K 2013 Scanning gate microscopy of localized states in wide graphene constrictions *Phys. Rev.* B **87** 085446
[41] Connolly M R, Chiou K L, Smith C G, Anderson D, Jones G A C, Lombardo A, Fasoli A and Ferrari A C 2010 Scanning gate microscopy of current-annealed single layer graphene *Appl. Phys. Lett.* **96** 113501
[42] Connolly M R, Puddy R K, Logoteta D, Marconcini P, Roy M, Griffiths J P, Jones G A C, Maksym P A, Macucci M and Smith C G 2012 Unraveling quantum Hall breakdown in bilayer graphene with scanning gate microscopy *Nano Lett.* **12** 5448–54
[43] Giesbers A J M, Zeitler U, Neubeck S, Freitag F, Novoselov K S and Maan J C 2008 Nanolithography and manipulation of graphene using an atomic force microscope *Solid State Commun.* **147** 366–9
[44] Jalilian R, Jauregui L A, Lopez G, Tian J, Roecker C, Yazdanpanah M M, Cohn R W, Jovanovic I and Chen Y P 2011 Scanning gate microscopy on graphene: charge inhomogeneity and extrinsic doping *Nanotechnology* **22** 295705
[45] Dou Z *et al* 2018 Imaging bulk and edge transport near the Dirac point in graphene Moiré superlattices *Nano Lett.* **18** 2530–7
[46] Tarucha S and Horihoshi Y 1992 Bend resistance characteristics of macroscopic four-terminal devices with a high elecrton mobility *Phys. Rev.* B **45** 13465–8
[47] Hirayama Y, Saku T, Tarucha S and Horikoshi Y 1998 Ballistic electron transport in macroscopic four-terminal square structures with high mobility *Appl. Phys. Lett.* **58** 2672
[48] Nyakiti L O, Wheeler V D, Garces N Y, Myers-Ward R L, Eddy C R and Gaskill D K 2012 Enabling graphene-based technologies: toward wafer-scale production of epitaxial graphene *MRS Bull.* **37** 1149–57
[49] Koon D W, Wang F, Petersen D H and Hansen O 2014 Sensitivity of resistive and Hall measurements to local inhomogeneities: finite-field, intensity, and area corrections *J. Appl. Phys.* **116** 133706
[50] Koon D W and Knickerbocker C J 1992 What do you measure when you measure resistivity? *Rev. Sci. Instrum.* **63** 207–10
[51] Mackenzie D M A and Peterson D H Unpublished result
[52] Panchal V, Pearce R, Yakimova R, Tzalenchuk A and Kazakova O 2013 Standardization of surface potential measurements of graphene domains *Sci. Rep.* **3** 2597
[53] Panchal V *et al* 2018 Confocal laser scanning microscopy for rapid optical characterization of graphene *Commun. Phys.* **1** 83
[54] Rajkumar R K, Asenjo A, Panchal V, Manzin A and Kazakova O 2015 Magnetic scanning gate microscopy of graphene Hall devices (invited) *J. Appl. Phys.* **115** 172606
[55] Barbolina I I, Novoselov K S, Morozov S V, Dubonos S V, Missous M, Volkov A O, Christian D A, Grigorieva I V and Geim A K 2006 Submicron sensors of local electric field with single-electron resolution at room temperature *Appl. Phys. Lett.* **88** 8–11
[56] Gilbertson A M, Sadeghi H, Panchal V, Kazakova O, Lambert C J, Solin S A and Cohen L F 2015 Multifunctional semiconductor micro-Hall devices for magnetic, electric, and photo-detection *Appl. Phys. Lett.* **107** 233504
[57] Gramse G, Kasper M, Fumagalli L, Gomila G, Hinterdorfer P and Kienberger F 2014 Calibrated complex impedance and permittivity measurements with scanning microwave microscopy *Nanotechnology* **25** 145703
[58] Varchon F *et al* 2007 Electronic structure of epitaxial graphene layers on SiC: effect of the substrate *Phys. Rev. Lett.* **99** 126805
[59] Ohta T, Bostwick A, Seyller T, Horn K and Rotenberg E 2006 Controlling the electronic structure of bilayer graphene *Science* **313** 951–5
[60] Santos E J G and Kaxiras E 2013 Electric-field dependence of the effective dielectric constant in graphene *Nano Lett.* **13** 898–902
[61] Lee D S, Riedl C, Krauss B, Von Klitzing K, Starke U and Smet J H 2008 Raman spectra of epitaxial graphene on SiC and of epitaxial graphene transferred to $SiO_2$ *Nano Lett.* **8** 4320–5